LAWRENCE
LIVERMORE
NATIONAL
LABORATORY

UCRL-JRNL-215631

Structure, Stability and Elm Dynamics of the H-Mode Pedestal in DIII-D

M. E. Fenstermacher, T. H. Osborne, A. W. Leonard, P. B. Snyder, D. M. Thomas, J. A. Boedo, T. A. Casper, R. J. Groebner, M. Groth, M. A. H. Kempenaars, A. Loarte, G. R. McKee, W. M. Meyer, G. Saibene, M. A. VanZeeland, X. Q. Xu, L. Zeng

September 23, 2005

Nuclear Fusion

Disclaimer

This document was prepared as an account of work sponsored by an agency of the United States Government. Neither the United States Government nor the University of California nor any of their employees, makes any warranty, express or implied, or assumes any legal liability or responsibility for the accuracy, completeness, or usefulness of any information, apparatus, product, or process disclosed, or represents that its use would not infringe privately owned rights. Reference herein to any specific commercial product, process, or service by trade name, trademark, manufacturer, or otherwise, does not necessarily constitute or imply its endorsement, recommendation, or favoring by the United States Government or the University of California. The views and opinions of authors expressed herein do not necessarily state or reflect those of the United States Government or the University of California, and shall not be used for advertising or product endorsement purposes.

STRUCTURE, STABILITY AND ELM DYNAMICS OF THE H–MODE PEDESTAL IN DIII–D

M.E. Fenstermacher,* T.H. Osborne, A.W. Leonard, P.B. Snyder, D.M. Thomas, J.A. Boedo,† T.A. Casper,* R.J. Groebner, M. Groth,* M.A.H. Kempenaars,‡ A. Loarte,§ G.R. McKee,◊ W.M. Meyer,* G. Saibene,‡ M.A. VanZeeland, X.Q. Xu,‡ L. Zeng,£ and the DIII–D Team

General Atomics
San Diego, California
United States of America

e-mail contact of main author: max.fenstermacher@gat.com

ABSTRACT. Experiments are described that have increased understanding of the transport and stability physics that set the H–mode edge pedestal width and height, determine the onset of Type-I edge localized modes (ELMs), and produce the nonlinear dynamics of the ELM perturbation in the pedestal and scrape-off layer (SOL). Models now exist for the n_e pedestal profile and the p_e height at the onset of Type-I ELMs, and progress has been made toward models of the T_e pedestal width and nonlinear ELM evolution. Similarity experiments between DIII–D and JET suggested that neutral penetration physics plays an important role in the relationship between the width and height of the n_e pedestal. Plasma physics appears to dominate in setting the T_e pedestal width. Measured pedestal conditions including edge current at ELM onset agree with intermediate-n peeling-ballooning (P-B) stability predictions. Midplane

* Lawrence Livermore National Laboratory, Livermore, California, USA
† University of California, San Diego, California, USA
‡ FOM-Rijnhuizen, Assoc. Euratom-FOM, TEC, Nieuwegein, Netherlands
§ EFDA-CSU, Max-Planck-Institut for Plasmaphysik, Garching, Germany
◊ University of Wisconsin, Madison, Wisconsin, USA
£ University of California Los Angeles, Los Angeles, California, USA

ELM dynamics data show the predicted (P-B) structure at ELM onset, large rapid variations of the SOL parameters, and fast radial propagation in later phases, similar to features in nonlinear ELM simulations.

PACS: 52.55.Fa, 28.52.-s, 52.35.Py

I. INTRODUCTION

This paper describes experiments that were focused on optimizing pedestal parameter measurements to determine, (1) the transport and stability physics that set the H–mode edge pedestal width and height, (2) the onset conditions for Type-I edge localized mode (ELM) instabilities, and (3) the nonlinear dynamics of the ELM perturbation observed in the pedestal and midplane scrape-off layer (SOL). These are three critical issues for future burning plasma devices such as ITER [1] because, for stiff profiles in the standard H–mode scenario, the height of the pedestal determines the overall confinement [2], and the size of the ELMs determines divertor target lifetimes [3]. The experiments were carried out primarily on DIII–D with additional results coming from dimensionally similar plasmas in DIII–D and JET.

Results are in agreement with models for the density pedestal width and the pressure gradient at the onset of Type-I ELMs, and show that progress has been made toward generating models of the temperature pedestal width (transport barrier) and nonlinear ELM evolution. Previous studies of pedestal structure have been done for many individual devices including MAST [4], C–Mod [5], ASDEX Upgrade (AUG) [6,7], JET [8] and DIII–D [9]. Recently pedestal structure has been examined through similarity studies between C–Mod/DIII–D [10] and between JET/JT–60U [11]. Studies of Type-I ELM evolution have also been reported from AUG [12–14], JET [15,16] and JT–60U [17,18] while studies of Type-III ELM evolution have been done at MAST [19,20] and TCV [21]. Studies have also been done on alternate small ELM regimes with good energy confinement such as the Type-II ELM regime in AUG [22], DIII–D [23] and JT60–U [24], the EDA regime in C–Mod [25], and the HRS regime in JFT-2M [26]. The new measurements reported in this paper show that the density pedestal width is consistent with neutral penetration physics playing a significant role in setting the density pedestal parameters. The pressure pedestal gradient is limited by the stability of coupled peeling-ballooning (P-B) instabilities at the edge. In similarity experiments with fixed pedestal beta, β, collisionality, ν^*, normalized gyroradius, ρ^* and safety factor, q, the transport barrier width,

Δ_T, scaled with minor radius, a. When $\rho*$ was varied at fixed $(\beta, \nu*, q)$, Δ_T/a was nearly independent of $\rho*$, and ELM size decreased as $\rho*$ decreased in agreement with changes in the radial mode width of the most unstable P-B mode. New edge current measurements confirmed the edge bootstrap current models used in the edge stability calculations. Finally, new fast data and initial nonlinear ELM simulations indicated that ELMs have a complicated spatial and temporal structure in the pedestal and SOL. Some initial scaling of these results to future devices is possible, as described below.

The paper is organized as follows. The experimental techniques and some of the important diagnostic measurements are described in Section 2. Experimental results are described in Section 3 including those from the pedestal similarity experiments, the edge stability characterization, and the nonlinear ELM dynamics. A summary and conclusions are given in Section 4.

II. EXPERIMENTAL TECHNIQUES AND DIAGNOSTICS

The pedestal transport and stability mechanisms were investigated both with new diagnostics in DIII–D and in similarity experiments with matched plasma shape and dimensionless pedestal parameters between DIII–D and JET. The similarity experiments focused on determining the physics mechanisms that set the pedestal widths. These were done in matched lower single-null (LSN) discharges with optimized shapes for pedestal profile diagnostics on JET (the so-called DOC-L shape with elongation κ = 1.72 and average triangularity, δ_{avg} = 0.27 and the DOC-U shape with κ = 1.68 and δ_{avg} = 0.35) [27,28]. For JET, typical discharge parameters were plasma current I_p = 1.2–2.5 MA, major radius R = 2.95 m, minor radius a = 0.93 m, and heating power in the range P_{inj} = 4.9–17.0 MW. For the pedestal similarity experiments, the dimensionless parameters $\beta \propto nT/B_T^2$, effective collisionality, $\nu* \propto nqRA^{3/2}/T^2$, effective Larmor radius, $\rho \propto T^{1/2}/a\ B_T$ and safety factor, $q \propto a^2 B_T/RI_p$ were matched at the top of the pedestal, although they could not be matched across the entire transport barrier profile. Here B_T

is the toroidal field, q is the safety factor at 95% flux, n and T are the density and temperature respectively, and A is the aspect ratio, R/a. In discharges with matched shape, maintaining fixed β, ρ^*, ν^*, and q at the top of the pedestal requires that density, temperature, toroidal field, and plasma current scale as $n_{ped} \propto a^{-2}$, $T^{ped} \propto A^{5/4} a^{-1/2}$, $B_T \propto A^{5/8} a^{-5/4}$, and $I_p \propto A^{-3/5} a^{-1/4}$ respectively. Studies of ρ^* dependence were done by varying B_T. In this case with fixed q, maintaining fixed β and ν^* at the top of the pedestal requires that $n^{ped} \propto A^{-5/6} a^{-1/3} B_T^{4/3}$, $T^{ped} \propto A^{5/6} a^{1/3} B_T^{2/3}$ and $I_p \propto A^{-1} a B_T$. Toroidal field was varied in JET from B_T = 1.2 to 2.7 T. Parameters in the DIII–D similarity discharges were I_p = 0.56–1.38 MA, R = 1.7 m, a = 0.6 m, P_{inj} = 1.12–9.5 MW and B_T = 1.0 to 2.1 T. Pedestal profiles were measured in JET with an edge LIDAR system (n_e and T_e) and with ECE emission (T_e). On DIII–D, profiles of n_e and T_e were measured with Thomson scattering. The profiles of ion temperature T_i were obtained from charge-exchange recombination (CER) spectroscopy.

Pedestal stability physics studies on DIII–D combined detailed pedestal plasma profile measurements with pedestal current density measurements using a unique new Li-beam polarimetry diagnostic [29] to predict the onset of ELMs from a linear peeling-ballooning theory with all relevant parameters measured. In these studies the plasma shape was optimized for pedestal and near SOL profile measurements with the DIII–D Thomson scattering and CER systems. Small radial excursions of the separatrix were used to further refine the profile measurements. In addition, for the first time the pitch angle of the magnetic field in the pedestal region was directly measured [29] simultaneously with the profiles using polarimetry of an injected lithium beam. This allowed the edge current density to be calculated directly from the Li-beam measurement using Ampere's Law. Combining magnetics measurements with the measured n_e, T_e, n_i T_i, and edge current density provided all the necessary parameters to generate accurate equilibrium reconstructions and to check theories of bootstrap current generation at the edge and peeling-ballooning stability predictions of ELM onset.

Pedestal dynamics during ELMs were measured on DIII–D with simultaneous fast diagnostics near the outer midplane. These included a tangentially viewing radial array of fast D_α detectors at up to 100 kHz [30], a fast reciprocating probe with data acquisition rates of 200 kHz for n_e and T_e, and 1 MHz for I_{sat} [31,32], profile reflectometry measurements up to $n_e = 6\times10^{19}$ m^{-3} at 40 kHz rate [33,34], beam emission spectroscopy of radially and poloidally propagating density fluctuations with 1 MHz acquisition rate [35,36], and a very fast interferometer chord viewing radially in from the outer midplane with a 5 MHz sampling rate [37]. Tests of the relative timing between different diagnostic digitizers were done using simultaneous square wave input. The relative timing errors were within one clock period of the digitizer unless noted below.

III. EXPERIMENTAL RESULTS

A. Pedestal Structure

Data from similarity experiments between DIII–D and JET, Figs. 1 through 3, are consistent with neutral penetration physics playing an important role in setting the relationship between the width, Δ_n, and height, n_e^{ped} of the density pedestal. The limited data obtained so far cannot, however, rule out the possibility that ionized particle transport physics also plays an important role in setting the density pedestal as suggested by previous studies [6,13]. These experiments were motivated by the results of previous pedestal similarity experiments between DIII–D and C–Mod [10] in which similar Δ_n/a was found in the two devices. Although this early result appeared to show that ionized particle transport physics was playing the most important role in setting the density pedestal width, models of neutral penetration effects [38–41] described below and applications to DIII–D profiles [42–44] suggested that the result could also be consistent with neutral sources playing an important role if the poloidal distribution of the neutral source was different in DIII–D and C–Mod.

For the present comparison between DIII–D and JET the dimensionless parameters β, ρ^*, ν^*, and q were well matched at the top of the pedestal in the similarity discharges for two different densities. The profiles of the dimensionless parameters for the low density case are shown in Fig. 1. The match at constant ρ^* is shown between a discharge in JET (black stars) and in DIII–D (red squares). Since the profiles evolve during the ELM cycle, achieving matched pedestal β, ρ^* ,ν^* required that the DIII–D data be selected from a particular time window during the ELM cycle when the pedestal parameters were the same as in the JET single time measurement. The JET profiles are from a point in time 58% of the inter-ELM time after an ELM crash. DIII–D multi-pulse Thomson scattering data, from a number of ELM cycles during the H–mode phase with constant macroscopic parameters, are shown for a window of 40%–60% of the ELM cycle. Estimates of the statistical error associated with the DIII–D Thomson scattering measurements are shown. A detailed error analysis including both systematic and statistical errors has not been done for either the DIII–D or the JET data. The location of the separatrix on each plot is that radial position corresponding to one-half of the temperature profile width outboard of the maximum gradient point of the hyperbolic tangent fit to the T_e profile, following Ref. [45]. The match of β, ρ^*, ν^* is very good at the top of the pedestal and q is matched within 5%. A similarly high quality match was achieved between measurements from a higher density discharge in JET (at 38% of the ELM cycle) and data from a higher density DIII–D discharge in a window of 20%–40% of the ELM cycle.

The widths of the temperature pedestals were similar in DIII–D and JET, both for the low density and high density cases, but the density pedestal width varied between the devices and with different densities (Figs. 2 and 3). For matched shapes and dimensionless parameters in the similarity discharges, normalized flux is equivalent to linear real space scaling of the profile dimensions. Figures 2(a) and 3(a) show that, although the top of the n_e pedestal in JET could not be determined precisely, the top of the n_e pedestal in DIII–D appeared to be further outboard than in JET for both densities. In the higher density similarity plasmas [Fig. 3(a)], the density

pedestal width appeared to be narrower, scaling as $\Delta_{ne} \sim 1/n_e^{ped}$ in both DIII–D and JET. Further experiments are planned to increase the coverage of the density pedestal at low density, in particular, in order to verify this apparent scaling. For both of the density cases the temperature profile widths [Figs. 2(b) and 3(b)] were very nearly the same in DIII–D compared with JET. The top of the temperature pedestal was inboard of the density pedestal in DIII–D [Figs. 2(a,b) and 3(a,b)]. The n_e and T_e profiles were more nearly aligned in JET.

Simulations of the density profiles using a neutral penetration model [38–41] reproduced the shape of the profiles including the difference between the two machines in the radial location of the top of the density pedestal [Fig. 2(a)] and the narrowing of the density pedestal with increasing density [Fig. 3(a)]. The neutral penetration model is based on a 1D fluid transport formulation in which the particle diffusion is balanced by neutral ionization in the pedestal and SOL. It takes into account Franck-Condon neutrals and the effect of poloidal variation in the neutral source due to differences in flux expansion around the SOL. Particle diffusivity within the closed flux surfaces is assumed constant and radial convective flux is assumed negligible compared with the diffusive flux. The model is valid in regimes for which T_e, within an ionization mean free path, is in the range of a few tens to a few hundred electron volts. This condition is typically satisfied for the edge plasmas in the similarity experiments except for the very lowest density cases not considered here.

To compute real density profile values from the model requires specification of three free parameters: (1) the flux expansion weighted by the neutral source, E^*, (2) the diffusivity coefficient on the closed flux surfaces, D_{SOL}, and (3) the population ratio, w, of neutrals at Frank-Condon (FC) energies versus those at the local ion energy due to multiple charge-exchange (CE) events. These were obtained [41] by fitting the model to a dataset of density pedestal widths versus pedestal density from a variety of DIII–D lower single-null discharges. The value of E^* is sensitive to the low density, large width part of the dataset from ohmic and L–mode plasmas, where FC neutrals dominate. Fitting to the DIII–D database produced a value

of $E^* = 7$, indicating that for DIII–D diverted equilibria shapes the neutral source comes from a broad region in the vicinity of the X-point. The value of D_{SOL} was determined from higher density H–mode plasmas where CE neutrals dominate. The best fit of the model to the DIII–D database was achieved with $D_{SOL} = 0.72$ m^2/s. Finally, the population ratio w is a sensitive function of the poloidal distribution of the sources and details of the SOL and divertor plasmas. Based on DIII–D data [42–44], the model [41] uses an estimate of this ratio derived by assuming the neutrals traverse a one-dimensional divertor plasma with parameters derived from the upstream separatrix density using a 1D conduction limited SOL model. This SOL assumption gives the well-known result that the divertor density increases as the cube of the upstream separatrix density and the divertor temperature decreases quadratically with increasing upstream density. With this formulation, the population ratio of CE versus FC neutrals was calculated using the experimentally measured upstream separatrix density and temperature combined with known functions for the CE and ionization rates versus density and temperature. The neutral population was dominated by charge-exchange neutrals for all cases except the lowest density plasmas at high ρ^* in the ρ^* scan. For DIII–D, the neutral energy at any point in the pedestal was assumed to be equal to the ion energy measured by the CER system. The model is sensitive to the neutral energy at the separatrix. For DIII–D the ion energy dropped by about a factor of 2 from the top of the pedestal to the separatrix, as can be seen by comparing Figs. 1(c) and 2(b). This factor of 2 decrease is roughly consistent with extrapolation of the measured DIII–D T_i profile from the top of the pedestal to the separatrix at constant gradient. For JET, where central T_i measurements were available only out to the top of the pedestal, the separatrix T_i was estimated from T_i at the top of the pedestal and the pedestal T_e profile by assuming the same profile of T_e/T_i as measured for DIII–D [Fig. 1(c)]. The neutral energy at the separatrix in the penetration model was assumed to be equal to this estimated separatrix ion energy for JET.

Using fixed values of $E^* = 7$ and $D_{SOL} = 0.72$ m^2/s, and calculating w from the measured upstream separatrix density and temperature for both the DIII–D and JET similarity discharges,

the predicted density profiles matched the measurements at both densities [Figs. 2(a) and 3(a)]. The model predicts that the width of the density pedestal should scale as the inverse of the density at the top of the pedestal, $\Delta_{ne} \sim 1/n_e^{ped}$, in agreement with the observations. The observed differences in the radial location between the n_e barriers [Figs. 2(a) and 3(a)] and the T_e barriers [Figs. 2(b) and 3(b)] suggest that physics other than neutral penetration dominates in setting the T_e barrier.

Plasma physics that scales with dimensionless parameters appears to dominate in setting the temperature pedestal width (transport barrier), Δ_T. Some theories suggest that neutral penetration also sets the temperature pedestal width [46]. If this were the case then Δ_T/a would scale as minor radius. However, in these pedestal similarity experiments, Δ_T/a was the same in both machines [Fig. 2(b)], suggesting that plasma physics, not neutral penetration controls the transport barrier width. A similar observation was made in DIII–D/C–Mod similarity experiments [47,48]. Also consistent with this interpretation was that $\Delta_T/a \sim$ constant was true for a range of densities [Figs. 2(b) and 3(b)].

No obvious variation of Δ_T/a with ρ^* was seen for fixed (β, ν^*, q) at the top of the pedestal during scans of B_T in DIII–D and JET. A factor of 1.6 variation of ρ^* was obtained in DIII–D for fixed (β, ν^*, q) by varying B_T from 1.0 to 2.1 T. So far only a 15% variation in ρ^* was achieved in JET during the pedestal similarity experiments. Future planned experiments should reduce ρ^* by almost a factor of 2 in JET, giving a total range of a factor of 4 for the combined dataset. An example from DIII–D with a ρ^* variation of 1.6 is shown in Figs. 1 and 2 by comparing data in red squares versus data in green crosses. Figure 1 shows a good match of β, ν^*, and q at the top of the pedestal for the two DIII-D cases at different ρ^*. In addition, T_e/T_i is also well matched. One dimensionless quantity that was not matched in the ρ^* scan was the toroidal Mach number in the pedestal [Fig. 1(f)]. The possible effect of the difference in toroidal rotation on the pedestal structure is under investigation. The profiles in Fig. 2(b) show that Δ_T/a does not vary between DIII–D and JET at the same ρ^*, nor does it vary as ρ^* is

changed by a factor of 1.5 in DIII–D. This result was obtained despite a significant change in Δ_n/a observed as $\rho*$ was varied in DIII–D [Fig. 2(a)]. For fixed $(\beta, \nu*, q, A, a)$, $n^{ped} \propto B_T^{4/3}$, and $\rho* \propto B_T^{2/3}$ so the reduction of Δ_n/a in the DIII–D case with reduced $\rho*$ is consistent with reduced neutral penetration at higher n^{ped}. This suggests that the physics mechanisms controlling Δ_T are different than those controlling Δ_n.

B. Pedestal Stability

Measured ELM onset conditions compared favorably with ELITE intermediate-*n* peeling-ballooning stability constraints calculated in self-consistent equilibria using the measured pedestal plasma profiles and a model for the edge current density, j^{edge}, that was constrained by new j^{edge} measurements (Fig. 4). First direct measurements [10,49] of the poloidal field in the pedestal were made at the outer midplane with a new Li-beam polarimetry diagnostic [50,51]. As an example, Fig. 4(a) shows the poloidal field profile in a lower single null discharge averaged over the last 150 ms prior to the first ELM during the ELM-free H–mode phase. Although the sampling rate of the Li-beam polarimeter can be as high as 300 kHz, this data was averaged over 150 ms to maximize the signal-to-noise ratio. The inferred j^{edge} [Fig. 4(b)] was consistent with calculations of edge Pfirsch-Schluter and bootstrap currents [52], using the measured pedestal plasma profiles and the NCLASS bootstrap model [53]. Free boundary equilibria that were constrained by the measured j^{edge}, were generated by the equilibrium solver in the CORSICA code [54]. The inverse solver in CORSICA provided an equilibrium solution in (ρ, θ) (i.e., poloidal flux, poloidal angle) with high midplane radial and X-point poloidal resolutions using an optimized, non-uniform grid. Linear stability calculations of ELM onset conditions were done on this equilibrium with the ELITE code [55–57]. In contrast to ELITE calculations for conditions between ELMs that show stability, for these plasma conditions just before ELM onset, ELITE showed instability for the high n = 30–35 modes, stability for low $n \leq 15$, and marginal stability for intermediate n modes, $16 \leq n \leq 29$. The mode structure for the most unstable mode in this case, n = 25 is shown in Fig. 5.

The dependence of the normalized ELM energy loss ($\Delta W_{ELM}/W_{ped}$), in the DIII–D ρ^* scan from the similarity experiments, was consistent with predicted changes in the peeling-ballooning mode width at the edge, but neutral penetration physics also played a role. As ρ^* decreased (Fig. 6) the steep gradient region in the measured pressure profile narrowed. The measured plasma profiles before and after ELMs also showed a narrower ELM affected region and reduced ELM energy loss at low ρ^*. In addition, the duration of the ELM magnetic fluctuations and their amplitude was smaller at low ρ^*. For the narrower pressure gradient region in the low ρ^* case, the calculated edge bootstrap current profile in the equilibrium reconstruction was narrower than at higher ρ^*. Combining these in the peeling-ballooning stability calculation produced a higher toroidal mode number for the most unstable mode and, consequently, a prediction of a narrower ELM onset region at low ρ^*. For these similarity experiments, the discharges at reduced ρ^* (by increased B_T) also were at higher density, $n_{ped} \sim B_T^{4/3}$ for fixed β, ρ^*, ν^*, q, A and a. Therefore, the narrowing of the steep gradient of the pressure was due in part to reduced neutral penetration at high density in this ρ^* scan.

C. ELM Dynamics in the Pedestal and Midplane SOL

Midplane and SOL ELM dynamics measurements show large, rapid variations of the SOL parameters and suggest a filamentary structure of the perturbation with fast radial propagation in later phases, and parallel propagation of the ELM pulse at speeds approaching the sound speed of pedestal ions. Previous measurements [58] confirmed the expected outer midplane dominated peeling-ballooning spatial structure at ELM onset. A reduction of n_e^{ped} was seen at all densities during an ELM and T_e^{ped} was also reduced at low n_e^{ped} ("conductive" ELMs) but no change to T_e^{ped} was seen during ELMs at high density ("convective" ELMs) [59,60]. Scanning reflectometer data show that the particles lost from the pedestal during an ELM appear far out in the SOL at the midplane [61,62]. This result was independent of the pre-ELM density. In the far outer SOL where n_e^{SOL} increases substantially, no increase in T_e^{SOL} was observed, implying rapid parallel conduction of the ELM energy in the SOL. Fast CER measurements showed

similar loss of impurities from the pedestal, a drop in pedestal toroidal and poloidal rotation, and the elimination of the pedestal electric field well by the ELM crash [63]. Scanning probe data near the separatrix showed large, rapid variations of both n_e^{SOL} and T_e^{SOL} during ELMs suggesting a filamentary structure of the perturbation [64]. This interpretation was supported by recent data from an ultra-fast radial interferometer chord (Fig. 7) At the time of the midplane D_α response to the ELM crash, the line integrated density at the midplane showed a burst of high frequency oscillations for $\approx 100\ \mu s$, consistent with the duration of the ELM perturbation on the fast magnetics signals. Beam emission spectroscopy (BES) data (Fig. 8) [64] also showed the development of a poloidally localized density "finger" that breaks away from the pedestal during the ELM crash. Finally, CIII (465 nm) visible emission data from a tangentially viewing fast-gated camera [65] at the midplane (Fig. 9), showed multiple filaments extended along the SOL flux surfaces. Toroidal mode number of these filaments, inferred from the CIII images, is $15 < n < 20$. ELITE calculations [Figs. 9(c,e)], for the case in Fig. 9(f), show a toroidal mode structure of the most unstable modes in the range $14 < n < 24$ at $q \sim 4$. CER measurements indicated that the ELM density perturbation structure might be toroidally rotating in the SOL [64,66]. The radial velocity of the density perturbation, inferred from both the probe and reflectometer data, was ~700 m/s near the separatrix. The radial velocity decreases with radius in the SOL. Parallel velocity of the density perturbation, inferred from the relative timing of the D_α pulses in the two divertors, approached the sound speed of ions at the pedestal temperature [67,68].

Poloidal and toroidal narrowing of the density perturbation into filaments (Figs. 10 and 11) were seen in nonlinear ELM simulations [69] with the BOUT code [70]. BOUT solves the 2-fluid Braginski equations in field line following coordinates. These simulations used input conditions consistent with those of a high density DIII–D discharge with small, convective ELMs. ELITE indicated that the starting conditions used in the non-linear simulations were beyond the linear instability threshold. The projection of the density perturbation, from all of the flux tubes in the simulation, onto a poloidal plane [Fig. 10(a)] in the linear phase of the mode

growth shows the outer midplane dominated structure of the perturbation expected from peeling-ballooning theory. At this stage the perturbation has a toroidal mode number, $n \sim 20$ [four lobes in one-fifth of the torus in Fig. 11(a)] and has a linear growth rate normalized to the Alfven frequency of $\gamma/\omega_A \sim 0.15$. When the growth becomes nonlinear, the density perturbation becomes more poloidally and toroidally localized [Fig. 11(b)]. At the ELM crash, the perturbation bursts into the SOL and breaks into filaments [positive and negative perturbation regions poloidally in Fig. 9(b) and local finger into the SOL in the midplane cut in Fig. 11(c)]. This is qualitatively consistent with nonlinear ballooning theory [71]. Although the simulations to date do not use the precise starting conditions of the measurements in Figs. 7, 8 or 9, they do show a substantial drop in the pedestal density, an increase in the far SOL density, and spatially localized structures of the density perturbation at the crash, all of which are qualitatively consistent with measurements.

IV. SUMMARY AND CONCLUSIONS

Progress has been made toward a quantitative physics understanding that will increase confidence in our ability to predict two critical aspects of future high-power tokamak operation, namely the width of the density pedestal and the pedestal pressure gradient at Type-I ELM onset. Some progress has also been made toward understanding the complex coupling of transport and stability mechanisms that set the temperature pedestal height and width. Given knowledge of n_e^{ped}, Δ_n predicted from a neutral penetration model agrees with present measurements in several experiments. This suggests that neutral penetration physics is playing an important role in determining the density pedestal width, although ionized particle transport in the pedestal must also be understood before predictions of the density pedestal can be made for future devices. The pedestal Δ_T appears to be dominated by plasma physics transport mechanisms not neutral penetration physics. The results suggest that it may be possible to independently influence Δ_n, by controlling fueling of the pedestal, either by controlling neutral sources from gas injection as in present devices or perhaps by optimizing particle deposition profiles from fueling systems

(*e*.g. pellets, compact toroid injection, etc.) in future devices. Independent control of the edge density profile at fixed temperature profile could allow optimization of the edge bootstrap current to minimize ELM energy loss for a given core confinement.

Linear peeling-ballooning stability calculations, using a model of the edge bootstrap current constrained by j^{edge} measurements, predict instability of intermediate-n peeling-ballooning modes for the measured pedestal pressure at ELM onset. They also predict that lower edge current might increase the toroidal mode number of the most unstable mode leading to smaller ELMs. Given that non-inductive current drive techniques have low efficiency in the plasma edge, the most promising approach to reducing the edge current and ELM size might be to fully understand the physics that independently controls the edge pedestal density and temperature gradients so that the edge bootstrap current can be optimized for a given core confinement as suggested above. Various techniques [72–77] that attempt to manipulate the edge profiles for ELM control are under investigation, including application of edge resonant magnetic fields [72–74], high frequency small pellets [75], and temporal magnetic triggering [76–77]. The reduction of measured ELM energy loss in DIII–D with decreasing $\rho*$ in the similarity experiments was consistent with increased n-number of the most unstable mode leading to narrower ELM affected region in the edge. For the inverse scaling of the density with $\rho*$ in these similarity experiments at fixed $(\beta, \nu*, q)$, this result was consistent with the neutral penetration model prediction that the density pedestal width (and, therefore, the edge bootstrap current width) should decrease as the density increased ($\rho*$ decreased). This suggests that tolerable sized ELMs may be possible in future devices at low $\rho*$ and high density if the high density operation leads to narrower density pedestal width and higher toroidal mode number of the ELM instability as it does in present gas-fueled experiments. In addition, the lack of $\rho*$ dependence of Δ_T/a also suggests favorable confinement in future devices with small $\rho*$. Finally, recent fast measurements of ELM dynamics in the midplane pedestal and SOL show evidence for a filamentary structure of the perturbation at the nonlinear ELM crash. Initial non-

linear fluid simulations show a poloidally and toroidally localized density perturbation at the crash, leading to a filamentary structure in the SOL that has qualitatively similar features to those seen in the data.

ACKNOWLEDGMENTS

This work was performed under the auspices of the U.S. Department of Energy by University of California Lawrence Livermore National Laboratory under Contract Nos. W-7405-ENG-48, DE-FC02-04ER54698, and Grant Nos. DE-FG02-04ER54758, DE-FG03-96ER54373, and DE-FG03-01ER54615.

REFERENCES

[1] ITER Physics Expert Groups, *ITER Physics Basis* 1999, Nucl. Fusion, **39** (1999) 2175.

[2] Osborne, T.H., *et al.*, Plasma Phys. and Control. Fusion **42** (2000) 1.

[3] Federici, G., *et al.*, J. Nucl. Mater. **313–316** (2003) 11.

[4] Kirk, A., *et al.*, Plasma Phys and Control. Fusion **46** (2004) A187

[5] Hughes, J., *et al.*, Phys. Plasmas **9** (2002) 3019.

[6] Nunes, I., *et al.*, "Study of the density pedestal width in ASDEX Upgrade using reflectometry," Proc. 31st EPS. Conf. on Plasma Physics and Controlled Fusion, London, UK, 2004 (ECA) P4-137.

[7] Horton, L.D., *et al.*, "Characterization of the H–mode Barrier in ASDEX-Upgrade," Proc. 20th IAEA Fusion Energy Conf., Villamoura, Portugal, 2004, EX/P3-4, to be published in Nucl. Fusion.

[8] Kallenbach, A., *et al.*, Plasma Phys and Control. Fusion **46** (2004) 431.

[9] Groebner, R.J., *et al.*, Plasma Phys and Control. Fusion **40** (1998) 673.

[10] Mossessian, D., *et al.*, Phys Plasmas, **10** (2003) 689.

[11] Saibene, G., *et al.*, Plasma Phys. and Control. Fusion **46** (2004) A195.

[12] Hermann, A., *et al.*, J. Nucl. Mater. **313–316** (2003) 759.

[13] Neuhauser, J., *et al.*, Plasma Phys. and Control. Fusion **44** (2002) 855.

[14] Nunes, I., *et al.*, Nucl. Fusion **44** (2004) 883.

[15] Ghendrih, P., *et al.*, J. Nucl. Mater. **313–316** (2003) 914.

[16] Goncalves, B., *et al.*, Plasma Phys. and Control. Fusion **45** (2003) 1627.

[17] Chankin, A.V., *et al.*, Nucl. Fusion **42** (2002) 733.

[18] Chankin, A.V., *et al.*, J. Nucl. Mater. **313–316** (2003) 828.

[19] Counsell, G., *et al.*, Plasma Phys. and Control. Fusion **44 (**2002**)** 827.

[20] Counsell, G., *et al.*, J. Nucl. Mater. **313–316** (2003) 804.

[21] R.A. Pitts *et al.*, Nucl. Fusion **43** (2003) 1145.

[22] Stober, J., *et al.*, Plasma Phys. and Contrl. Fusion **42**, (2000) A211-A216.

[23] Ozeki, T., *et al.* Nucl. Fusion **30** (1990) 1425.

[24] Kamada, Y., *et al.*, Plasma Phys. and Contrl. Fusion **38** (1996) 1387.

[25] Takase, Y., *et al.*, Phys. Plasmas **4**, (1997) 1647.

[26] Kamiya, K., *et al.*, Nucl. Fusion **43** (2003) 1214.

[27] Loarte, A., *et al.*, Phys. Plasmas **11** (2004) 2668.

[28] Kempenaars, M., *et al.*, "Edge gradient and pedestal measurements of ELMy H–mode plasmas in JET," Proc. 30th EPS Conf. on Control. Fusion and Plasma Phys., St. Petersburg, Russia, ECA Vol. 27A (2003) P1.92.

[29] Thomas, D.M., *et al.*, Phys. Rev. Lett. **93** (2004) 65003.

[30] Colchin, R.J., *et al.*, Rev. Sci. Instrum. **74** (2003) 2068.

[31] Boedo, J.A., *et al.*, Rev. Sci. Instrum. **69** (1998) 2663.

[32] Boedo, J.A., *et al.*, Rev. Sci. Instrum. **70** (1999) 2997.

[33] Zeng, L., *et al.*, Rev. Sci. Instrum. **74** (2003) 1530.

[34] Wang, G., *et al.*, Rev. Sci. Instrum. **74** (2003) 1525.

[35] McKee, G.R., *et al.*, Rev. Sci. Instrum. **70** (1999) 2179.

[36] McKee, G.R., *et al.*, Rev. Sci. Instrum. **74** (2003) 2014.

[37] VanZeeland, M.A., and Carlstrom, T.N., Rev. Sci. Instrum. **75** (2004) 3423.

[38] Wagner, F., and Lackner, K., Phys. Plasmas-Wall Interactions in Controlled Fusion, NATO ASI Series B, Physics (1986) Vol. 131, p. 931.

[39] Engelhardt, W. and Feneberg, W.J., J. Nucl. Mater. **76–77** (1978) 518.

[40] Mahdavi, M.A., *et al.*, Phys. Plasmas **10** (2003) 3988.

[41] Mahdavi, M.A., *et al.*, Nucl. Fusion **42** (2002) 52.

[42] Groebner, R.J. *et al.*, Plasma Phys. and Contrl. Fusion **44** (2002) A265.

[43] Groebner, R.J. *et al.*, Phys. Plasmas **9** (2002) 2134.

[44] Groebner, R.J. *et al.*, Nucl. Fusion **44** (2004) 204.

[45] Porter, G.D., *et al.,* Phys. Plasmas **5** (1998) 1410.

[46] Hinton, F.L., and Staebler, G.M., Phys. Fluids B **5** (1993) 1281.

[47] Mossessian, D.A., *et al.,* Phys. Plasmas **10** (2003) 1720.

[48] Mossessian, D.A., "H-mode pedestal physics studies in local dimensionless identity experiments," Proc. 30th EPS. Conf. on Plasma Physics and Controlled Fusion, St. Petersburg, Russia, 2003 (ECA) Vol. 27A, P3.182.

[49] Thomas, D.M., *et al.,* Proc. 31st EPS. Conf. on Plasma Physics and Controlled Fusion, London, UK, 2004 (ECA) Vol. 28G, P2.177.

[50] Thomas, D.M., *et al.*, Rev Sci. Instrum. **74** (2003) 1541.

[51] Thomas, D.M., *et al.*, Rev. Sci. Instrum. **75** (2004) 4109.

[52] Thomas, D.M., *et al.*, Phys. Plasmas **12** (2005) 056123.

[53] Houlberg, W.A., *et al.,* Phys. Plasmas **4** (1997) 3230.

[54] Casper, T.A., *et al.,* Proc. 30th EPS. Conf. on Plasma Physics and Controlled Fusion, St. Petersburg, Russia, 2003 (ECA) P3.207.

[55] Snyder, P.B., *et al.*, Phys. Plasmas **9** (2002) 2037.

[56] Snyder, P.B., *et al.,* Nucl. Fusion **44** (2004) 320.

[57] Wilson, H.R., *et al.*, Phys. Plasmas **9** (2002) 1277.

[58] Petrie, T.W., *et al.*, Nucl. Fusion **43** (2003) 910.

[59] Leonard, A.W., *et al.*, J. Nucl. Mater. **313–316** (2003) 768.

[60] Leonard, A.W., *et al.*, Phys. Plasmas **10** (2003) 1765.

[61] Zeng, L., *et al.*, Plasma Phys. Control. Fusion **46** (2004) A121.

[62] Zeng, L., *et al.*, J. Nucl. Mater. **337–339** (2004) 742.

[63] Wade, M.R., *et al.*, J. Nucl. Mater. **337–339**, (2005) 737.

[64] Boedo, J.A., *et al.*, "Edge localized mode dynamics and transport in the scrape-of layer of the DIII–D tokamak," Phys. Plasmas **12** (2005) 072516.

[65] Groth, M., *et al.*, Rev. Sci. Instrum. **74** (2003) 2064.

[66] Boedo, J.A., *et al.*, "ELM-induced plasma transport in the DIII–D SOL," Proc. 31st EPS. Conf. on Plasma Physics and Controlled Fusion, London, UK, 2004.

[67] Fenstermacher, M.E., *et al.*, Plasma Phys. Control. Fusion **45** (2003) 1597.

[68] Fenstermacher, M.E., *et al.*, J. Nucl. Mater. **337–339** (2004) 781.

[69] Snyder, P.B., Wilson, H.R., and Xu, X.Q., **12** (2005) 056115.

[70] Xu, X.Q., *et al.*, Nucl. Fusion **40** (2000) 731.

[71] Wilson, H.R., and Cowley, S.C., Phys. Rev. Lett. **92** (2004) 175006.

[72] Evans, T.E., *et al.*, Phys. Rev. Lett. **92** (2004) 235003.

[73] Moyer, R.A., *et al.*, Phys Plasmas **12** (2005) 056119.

[74] Evans, T.E., *et al.*, Nucl. Fusion **45** (2005) 595.

[75] Lang, P.T., *et al.*, Nucl. Fusion **44** (2004) 665.

[76] Degeling, A.W., *et al.*, Plasma Phys. Control. Fusion **45** (2003) 1637.

[77] Lang, P.T., *et al.*, Plasma Phys. Control. Fusion **46** (2004) L31-L39.

FIGURE CAPTIONS

Fig. 1. Profiles of electron beta, β_e (a), $log_{10}(\nu_e^*)$ (b), T_e/T_i (c), $\rho*$ (d), q (e) and toroidal Mach number of fully stripped carbon (f), as functions of normalized poloidal flux, are well matched in the pedestal for similarity plasmas at low density in JET (black stars) and DIII–D (red squares). For comparison a DIII–D case at high $\rho*$ (green crosses) from the $\rho*$ scan is also shown. Vertical lines indicate position of the separatrix (solid) and top of the temperature pedestal (dashed).

Fig. 2. Electron density profiles (a) and predictions from the neutral penetration model (curves) for the same lower density discharges shown in Fig. 1. Electron temperature profiles (b) and hyperbolic tangent fits (curves) show no significant difference in temperature barrier width between JET (black stars) and DIII–D (red squares), nor for variation of $\rho*$ in DIII–D (red squares versus green crosses). B_T (JET) = 1.2 T, B_T (DIII–D) = 2.1 T (red squares) and 1.0 T (green crosses). Density scaled to DIII–D as $n_e \propto a^{-1/3}A^{-5/6}B^{4/3}$; temperature scaled to DIII–D as $T_e \propto a^{1/3}A^{5/6}B^{2/3}$.

Fig. 3. Electron density profiles (a) and predictions from the neutral penetration model (curves) for the higher density discharges. Electron temperature profiles (b) again show no significant difference in temperature barrier width between JET (black stars) and DIII–D (red squares). Density and temperature scaled as in Fig. 2.

Fig. 4. Li-beam polarimetry measurements of the pedestal poloidal field profile (a), and the inferred edge current density profile (b), for plasma conditions just before ELM onset. The measured profiles (solid) are compared with calculated values using an equilibrium reconstruction code constrained by the NCLASS bootstrap current model (dotted), and with measured L–mode phase profiles (dashed). Separatrix position shown by solid vertical line and ρ = 0.83 surface shown by dashed vertical line. A significant increase in the edge current is seen

between L–mode and the profile in H–mode just before an ELM. The measured current density peak of 1.35 MA/m^2 agrees well with the calculated value.

Fig. 5. The ELITE prediction of the poloidal mode structure (density perturbation) for the most unstable mode in a kinetic equilibrium reconstructed using the edge current from Fig. 3 as a constraint. Positive perturbation is yellow, negative perturbation is black, no perturbation is red.

Fig. 6. Measured pressure gradient profile ($-d\beta/d\psi$, dotted), calculated normalized current profile [$\langle j_\phi \rangle/(I_p/\text{Area})$, dashed] and most unstable peeling-ballooning mode eigen functions for large ρ^* (a) and small ρ^* (b) from the DIII–D/JET similarity experiments. The ELM affected area is reduced for smaller ρ^*.

Fig. 7. Fast measurements of midplane dynamics during an ELM crash; (a) midplane and divertor D_α emission (a.u.), (b) line averaged midplane density from radial interferometer chord (10^{19} m^{-3}), (c) line averaged divertor density from a vertical interferometer chord (10^{19} m^{-3}), (d) dB/dt (T/s), (e) current integrated on divertor tile (A). Onset of midplane D_α response to the ELM crash marked by vertical dotted line. Two percent of the data points are marked with circles to indicate the temporal resolution.

Fig. 8. Deviation of density (red-positive, blue-negative) from average (white) near the poloidal midplane during an ELM crash. Snapshots (1 μs integration) at (a) 27 μs, (b) 33 μs and (c) 34 μs from the start of the midplane D_α response to the ELM crash show a highly poloidally localized filament that propagates radially into the SOL. Separatrix for Z = 0 at 225.6 cm (dashed line).

Fig. 9. CIII (465 nm) images with 10 μs exposure during ELM crashes and ELITE simulation results. (a) Camera view of vacuum vessel in reflected light, (b,d,f) images of CIII emission during different ELM crashes, (c) 2D profile of instability mode from ELITE for case shown in (f), and camera view of 3D mode structure from ELITE (e) for case (f).

Fig. 10. Density perturbation from multiple flux tubes in the pedestal and SOL projected onto a poloidal plane from (a) linear growth phase and (b) nonlinear crash phase of a BOUT nonlinear ELM simulation. Inset shows expansion of region near the outer midplane. Unperturbed density is in red, positive perturbation in yellow, and negative perturbation in blue. Dotted line shows the separatrix position.

Fig. 11. Density contours versus toroidal angle and radius from a BOUT nonlinear ELM simulation showing (a) instability mode structure during linear growth phase, (b,c) nonlinear growth of toroidally localized density perturbation and radial propagation at ELM crash. Data shown on a plan view of one-fifth of the torus at the outer equatorial midplane. Unperturbed density is in light blue, positive perturbation in purple-white, and negative perturbation in yellow-red. Color scale range indicated: $\pm 1\%\ n_e^{ped}$ in (a), $\pm 10\%\ n_e^{ped}$ in (b), $\pm 90\%\ n_e^{ped}$ in (c).

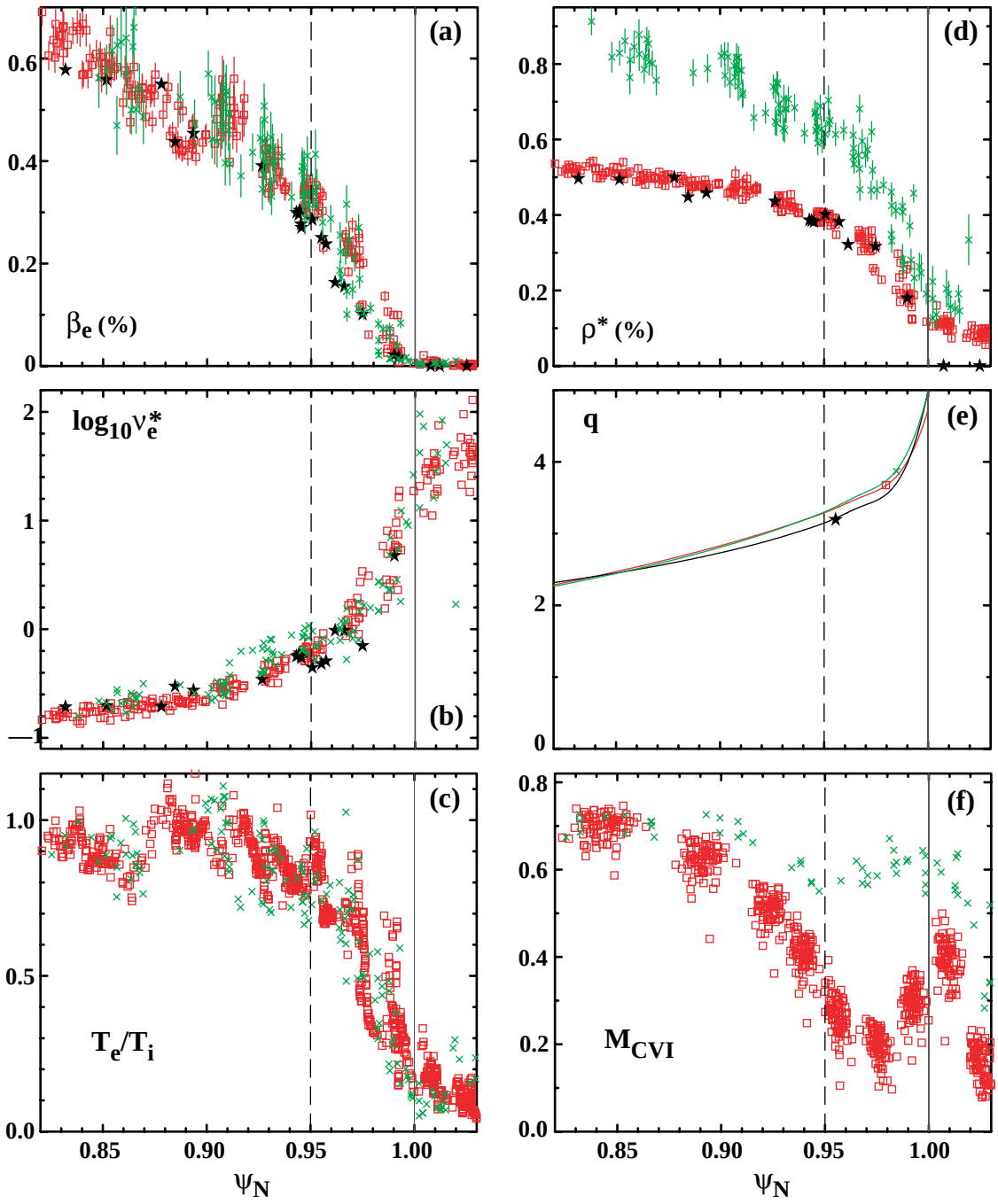

Fig. 1, M.E. Fenstermacher
NF/191430/PAP/70903

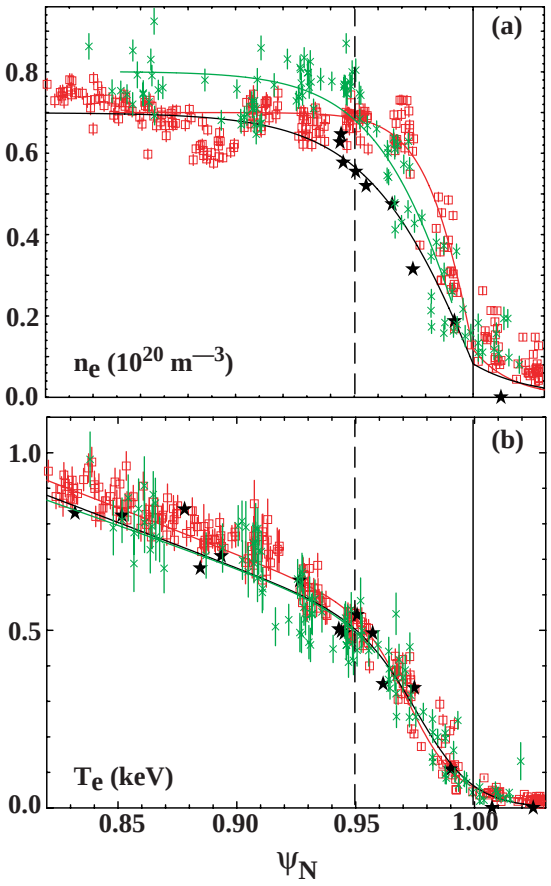

Fig. 2, M.E. Fenstermacher
NF/191430/PAP/70903

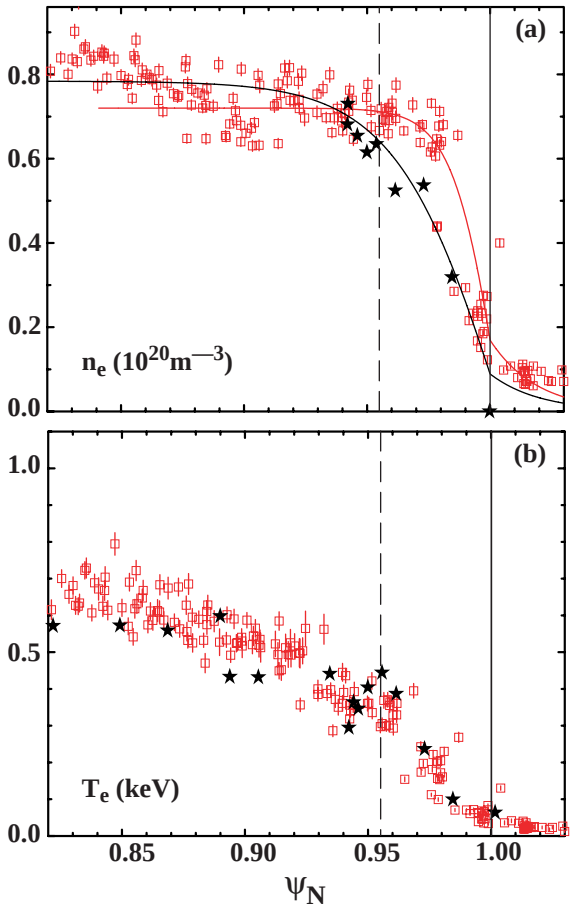

Fig. 3, M.E. Fenstermacher
NF/191430/PAP/70903

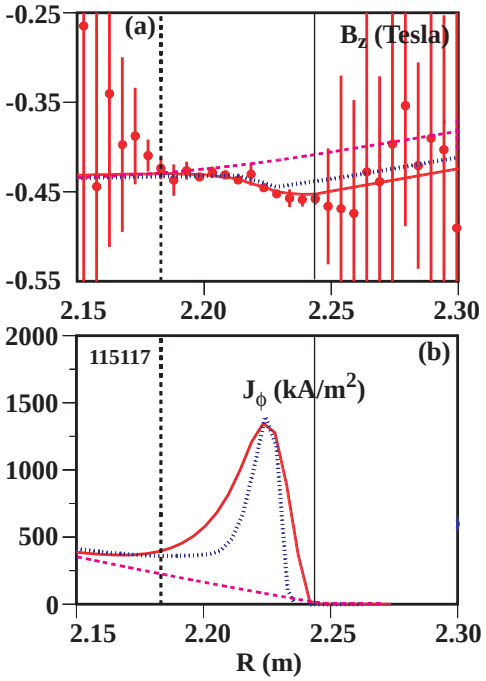

Fig. 4, M.E. Fenstermacher
NF/191430/PAP/70903

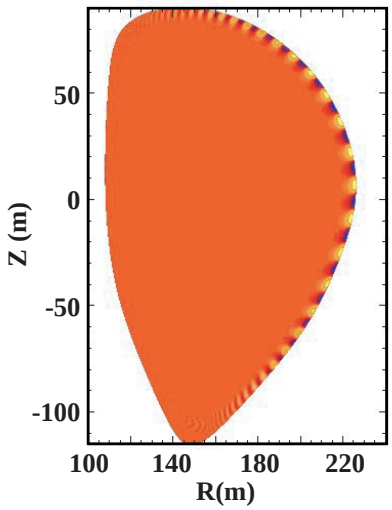

Fig. 5, M.E. Fenstermacher
NF/191430/PAP/70903

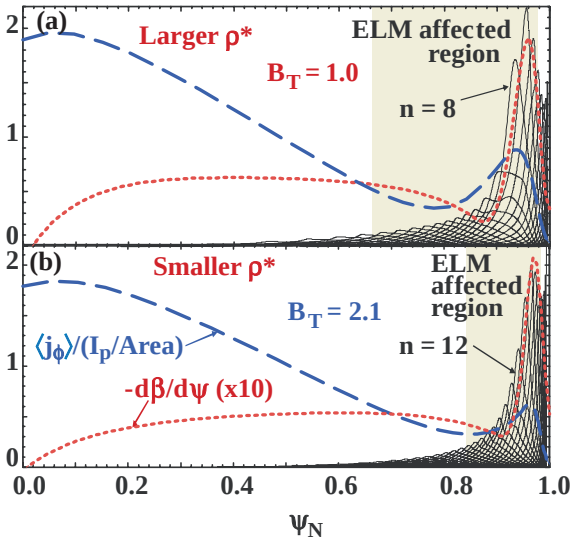

Fig. 6, M.E. Fenstermacher
NF/191430/PAP/70903

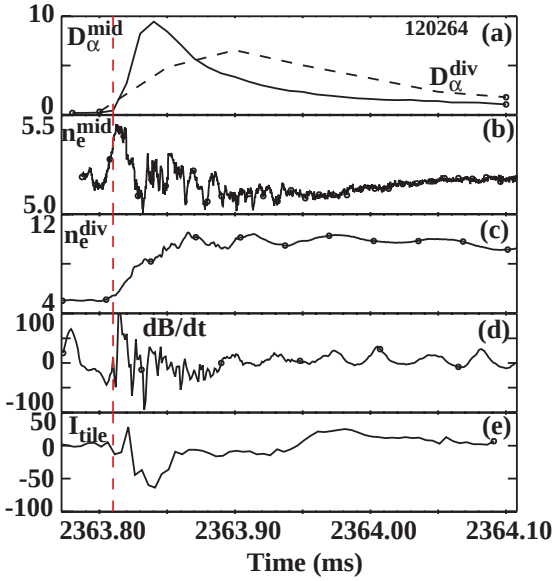

Fig. 7, M.E. Fenstermacher
NF/191430/PAP/70903

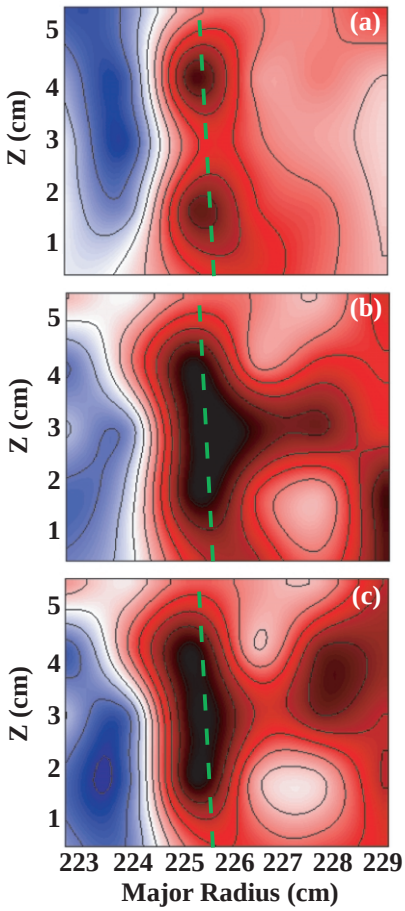

Fig. 8, M.E. Fenstermacher
NF/191430/PAP/70903

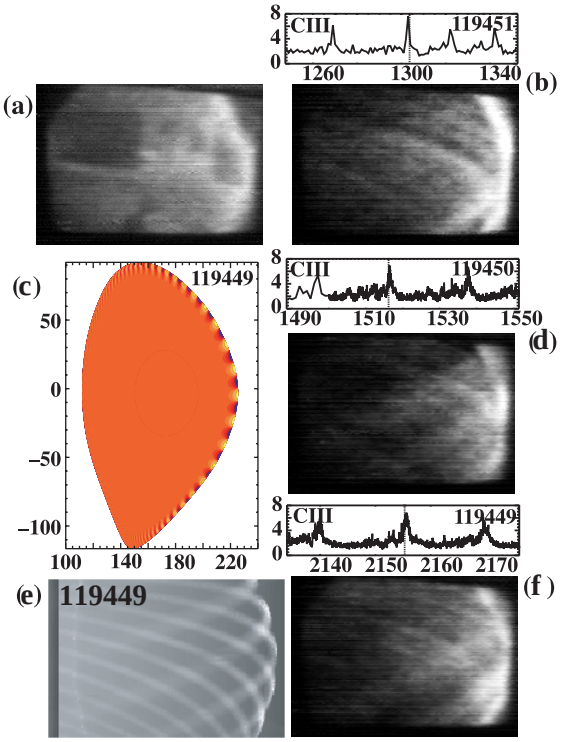

Fig. 9, M.E. Fenstermacher
NF/191430/PAP/70903

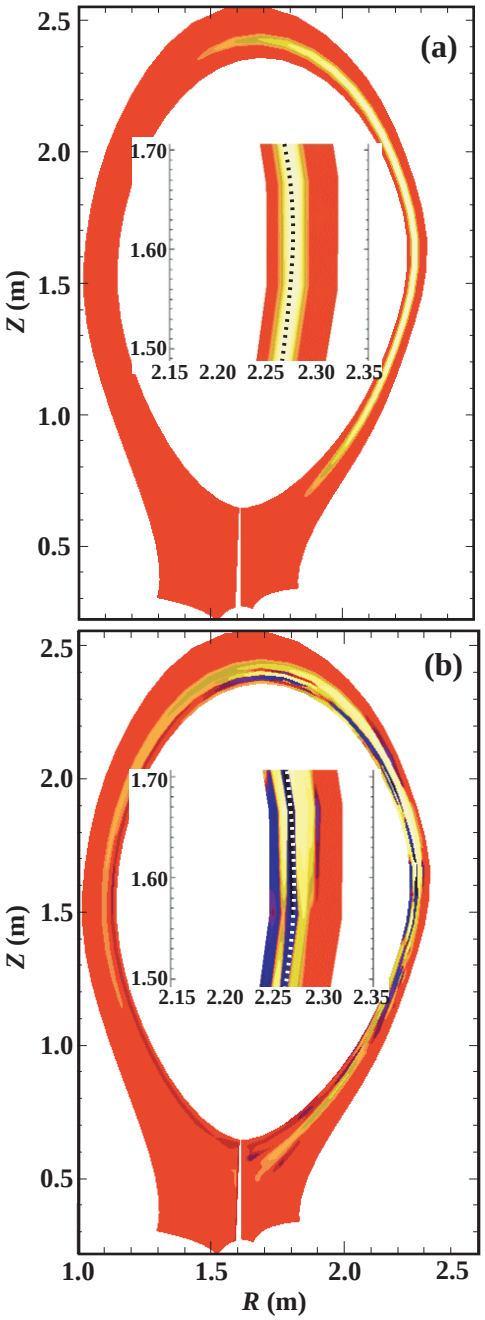

Fig. 10, M.E. Fenstermacher
NF/191430/PAP/70903

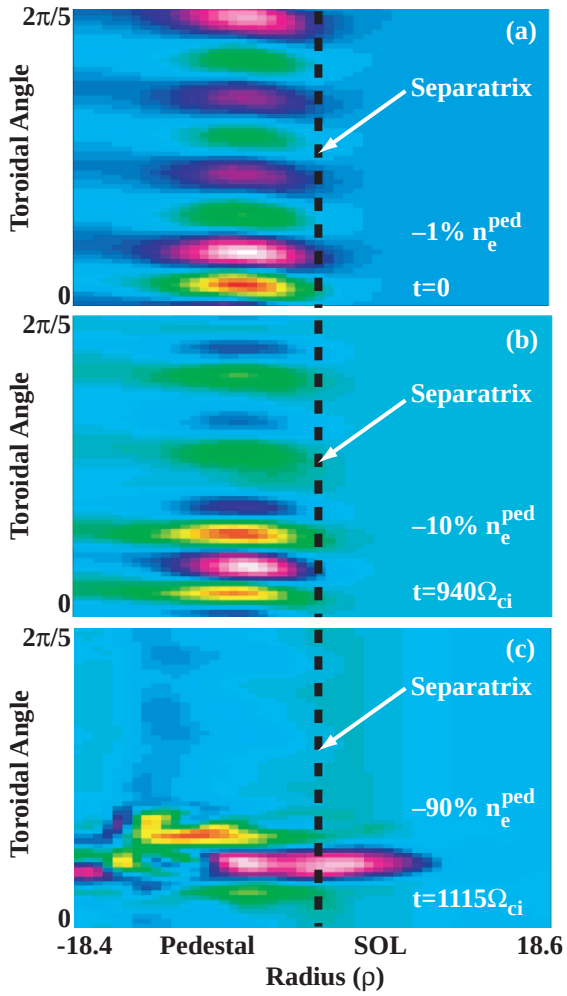

Fig. 11, M.E. Fenstermacher
NF/191430/PAP/70903